

Article

Theoretical Prediction and Experimental Synthesis of Zr_3AC_2 ($A = Cd, Sb$) Phases

Jia Luo ^{1,†}, Fengjuan Zhang ^{1,†}, Bo Wen ^{1,†}, Qiqiang Zhang ¹, Longsheng Chu ¹, Yanchun Zhou ^{2,*}, Qingguo Feng ^{1,*} and Chunfeng Hu ^{1,*} 

- ¹ Key Laboratory of Advanced Technologies of Materials, Ministry of Education, School of Materials Science and Engineering, Southwest Jiaotong University, Chengdu 610031, China; luojia07232000@163.com (J.L.); zjf6782022@163.com (F.Z.); swjtu202213@163.com (B.W.); zhangqiqiang@std.uestc.edu.cn (Q.Z.); lshchu@home.swjtu.edu.cn (L.C.)
- ² School of Materials Science and Engineering, Zhengzhou University, Zhengzhou 450001, China
- * Correspondence: yczhou@alum.imr.ac.cn (Y.Z.); qfeng@swjtu.edu.cn (Q.F.); chfhu@live.cn (C.H.)
- † These authors contributed equally to this work.

Abstract: MAX phases have great research value and application prospects, but it is challenging to synthesize the MAX phases containing Cd and Sb for the time being. In this paper, we confirmed the existence of the 312 MAX phases of Zr_3CdC_2 and Zr_3SbC_2 , both from theoretical calculations and experimental synthesis. The Zr_3AC_2 ($A = Cd, Sb$) phase was predicted by the first-principles calculations, and the two MAX phases were confirmed to meet the requests of thermal, thermodynamic, and mechanical stabilities using formation energy, phonon dispersion, and the Born–Huang criteria. Their theoretical mechanical properties were also systematically investigated. It was found that the elastic moduli of Zr_3CdC_2 and Zr_3SbC_2 were 162.8 GPa and 164.3 GPa, respectively. Then, differences in the mechanical properties of Zr_3AC_2 ($A = Cd, In, Sn, and Sb$) were explained using bond layouts and charge transfers. The low theoretical Vickers hardness of the Zr_3CdC_2 (5.4 GPa) and Zr_3SbC_2 (4.3 GPa) phases exhibited excellent machinability. Subsequently, through spark plasma sintering, composites containing Zr_3CdC_2 and Zr_3SbC_2 phases were successfully synthesized at the temperatures of 850 °C and 1300 °C, respectively. The optimal molar ratio of Zr:Cd/Sb:C was determined as 3:1.5:1.5. SEM and the EDS results analysis confirmed the typical layered microstructure of Zr_3CdC_2 and Zr_3SbC_2 grains.

Keywords: Zr_3CdC_2 ; Zr_3SbC_2 ; first-principles calculation; theoretical mechanical properties; synthesis



Citation: Luo, J.; Zhang, F.; Wen, B.; Zhang, Q.; Chu, L.; Zhou, Y.; Feng, Q.; Hu, C. Theoretical Prediction and Experimental Synthesis of Zr_3AC_2 ($A = Cd, Sb$) Phases. *Materials* **2024**, *17*, 1556. <https://doi.org/10.3390/ma17071556>

Academic Editors: Sergei A. Kulichin, Aleksandr Kuchmizhak, Mitsuhiro Honda and Valery A. Svetlichnyi

Received: 26 February 2024

Revised: 26 March 2024

Accepted: 26 March 2024

Published: 28 March 2024



Copyright: © 2024 by the authors. Licensee MDPI, Basel, Switzerland. This article is an open access article distributed under the terms and conditions of the Creative Commons Attribution (CC BY) license (<https://creativecommons.org/licenses/by/4.0/>).

1. Introduction

Nowotny discovered the H-phases in 1967, and Barsoum defined this kind of material as the $M_{n+1}AX_n$ phase (MAX phase) until 2000 [1–4]. $M_{n+1}AX_n$ phases are a family of hexagonal, ternary layered compounds. Generally, M-site elements are early transition metals, A-site elements mainly come from IIIA–VA elements, and X-site elements are C, N, or B. All MAX phases have a hexagonal crystal structure, and their space group belongs to $P6_3/mmc$. The X atom is located at the center of the octahedron composed of M atoms, and the entire crystal structure is composed of densely packed M_6X octahedron layers and A layers, which are alternated periodically. According to the difference in the number of M layers between two A layers, MAX phases can be generally divided into 211 ($n = 1$), 312 ($n = 2$), and 413 ($n = 3$) phases [5–13]. The MAX phase contains covalent, ionic, and metallic bonds and has both ceramic and metallic properties [14]. The strong covalent and ionic bonds between MX atoms contribute to the thermodynamic and mechanical stability of the MAX phase [15]. The weak covalent bonds and metal bonds exist between MA atoms, and metal bonds exist between MM atoms. The special nanolayered crystal structure endows them with a high elastic modulus, high strength, and excellent machinability, as well as high electrical conductivity and high thermal conductivity. Therefore, MAX phases are

promising to be high-temperature structural materials, electrode brush materials, chemical resistant materials, high-temperature heating materials, etc. [16,17].

Nowadays, MAX phases are becoming popular research materials due to their excellent properties and wide range of potential applications [18]. In recent years, more and more 312 MAX phases have been discovered and studied. For instance, 312 MAX phases containing In and Sn as A-position elements have been successfully synthesized recently. Lapauw et al. successfully synthesized Zr_3SnC_2 by spark plasma sintering with Fe, Co, or Ni additives in 2017 and proposed the mechanism for the synthesis of Zr_3SnC_2 [19,20]. Most recently, an indium-containing MAX phase of Zr_3InC_2 was also successfully sintered by spark plasma sintering [21]. In the periodic table of elements, Cd and Sb are in the same period of In and Sn, and these four elements are located next to each other. However, perhaps due to the challenging synthesis of MAX phases in which the A elements are Cd and Sb, we found that previous research reports on MAX phases containing Cd and Sb were uncommon. For example, Ti_2CdC was successfully sintered at 750 °C by Nowotny in 1964 [22]. The crystal structure, chemical bonding, and elastic properties of Ti_2CdC were investigated by first-principles calculations, and this cadmium-containing MAX phase was predicted to have potential applications as electric friction materials [23,24]. Therefore, theoretical prediction and experimental synthesis of Zr_3AC_2 ($A = Cd, Sb$) MAX phases is a necessary and meaningful endeavor. To the best of our knowledge, this article is the first report on Zr_3CdC_2 and Zr_3SbC_2 phases. The discovery of these two MAX phases may provide ideas for the synthesis of high-purity Zr_3CdC_2 and Zr_3SbC_2 phases and new options in the field of electrically and thermally conductive materials.

In this work, the new 312 MAX phases of Zr_3AC_2 ($A = Cd, Sb$) were predicted to be stable by using the first-principles calculations, and their basic mechanical properties were systematically calculated. Furthermore, by adopting spark plasma sintering, the Zr_3CdC_2 and Zr_3SbC_2 phases were successfully synthesized, and their laminar microstructures were well determined.

2. Experimental Procedures

2.1. First-Principles Calculation

In this work, all the calculations were performed by the density functional theory (DFT) calculations in a framework of generalized gradient approximation with the projector augmented-wave method implemented in the Vienna ab initio simulation package (VASP5.4.4, Hafner Group, University of Vienna, Vienna, Austria), where the Perdew–Burke–Ernzerhof (PBE) functional has been adopted for exchange-correlation potential [25,26]. The convergence criteria for energy and force were set to 10^{-6} eV and 0.01 eV/Å, respectively. The plane-wave basis set cutoff was 450 eV after the convergent test, and the special k-points sampling integration over the Brillouin zone was employed using the Monkhorst–Pack method with $12 \times 2 \times 2$ spatial k-points mesh. The elastic constants, mechanical moduli, and phonon dispersion were calculated through the finite displacement method. In order to obtain an accurate acoustic vibration mode, we first optimized the lattice structure of the MAX phase. Secondly, the mechanical constants were calculated using density functional perturbation theory (DFPT). Finally, lattice vibration and thermodynamic properties were extracted from the VASP output by the Phonopy post-processing 2.17.1 software. Because MAX phases had a layered structure, the van der Waals force was involved through the Grimme-D3 scheme to correctly address the interactions between layers. This method can more accurately describe the weak interaction between molecules by introducing additional van der Waals terms [27]. Additionally, the crystal structures of the Zr_3AC_2 ($A = Cd, Sb$) phases were visualized by using the VESTA-gtk3 software [28].

2.2. Synthesis of Zr_3CdC_2 and Zr_3SbC_2 Phases

Commercial powders of zirconium (99.5% purity, 500 mesh; Eno High-Tech Material Development Co., Ltd., Qinhuangdao, China), cadmium (99.5% purity, 300 mesh; Eno High-Tech Material Development Co., Ltd., China), antimony (99.9% purity, 500 mesh; Eno

High-Tech Material Development Co., Ltd., China), and graphite (99.95%, 500 mesh; Eno High-Tech Material Development Co., Ltd., China) were used as the initial materials. To successfully synthesize the Zr_3CdC_2 and Zr_3SbC_2 phases, different sintering temperatures and molar ratios were designed. The powders were weighed using an electric balance with an accuracy of 10^{-4} g and mixed in a plastic bottle for 12 h at 50 rpm. Then, the mixture was placed into a graphite die with a diameter of 20 mm. The sintering process was carried out in a spark plasma sintering furnace (SPS-20T-10, Shanghai Chenhua Technology Co., Ltd., Shanghai, China). The heating rate was $50\text{ }^{\circ}\text{C}/\text{min}$, and the applied pressure was 30 MPa. After sintering, the samples were cooled down to ambient temperature with the furnace. The surface contaminations of samples were removed by a diamond grinding wheel.

2.3. Composition and Microstructure Characterization

X-ray diffraction (XRD) (Ultima IV, Rigaku, Japan) with a Cu-K α radiation source in the 2θ range of $5\text{--}75^{\circ}$ was used for the composition analyses of the Zr_3CdC_2 and Zr_3SbC_2 phases. The theoretically calculated X-ray diffraction patterns of Zr_3CdC_2 and Zr_3SbC_2 were determined by the Materials Studio 8.0 software (Accelrys Software Inc., San Diego, CA, USA) using the optimized lattice parameters of Zr_3CdC_2 and Zr_3SbC_2 as the input. The microstructure features and elemental compositions of the fracture surfaces of sintered samples were monitored using a scanning electron microscope (SEM) (Apreo 2C, Thermo Fisher Scientific, Brno, Czech Republic) equipped with an energy dispersive spectroscope (EDS) (Oxford ultim Max 65, Oxford Ins., Oxford, UK).

3. Results and Discussion

3.1. Stability Calculation of Zr_3CdC_2 and Zr_3SbC_2 Phases

The crystal structures of experimentally synthesized Zr_3SnC_2 and Zr_3InC_2 are both $P6_3/mmc$ [19,21]. Since Cd, In, Sn, and Sb belong to the same period in the periodic table of the elements, it was predicted that the properties and crystal structures of Zr_3CdC_2 and Zr_3SbC_2 are similar to those of Zr_3SnC_2 and Zr_3InC_2 , and therefore, they were modeled and calculated according to the $P6_3/mmc$ space group. Figure 1 shows the crystal structures of two new 312 MAX phases of Zr_3CdC_2 and Zr_3SbC_2 . The optimized lattice parameters of Zr_3AC_2 ($A = Cd, In, Sn, Sb$) were calculated and are listed in Table 1. For comparison, the experimental parameters of two synthesized 312 phases of Zr_3InC_2 and Zr_3SnC_2 are also listed. It is clearly determined that when the M and X sites are identical, the planar lattice parameter a shows a monotonic increase from 3.319 to 3.367 Å with the increasing order of the atomic number of A-site elements, while the vertical lattice parameter c shows a decrease simultaneously from 20.393 to 19.413 Å, indicating that the bonds within the (0001) plane become weaker and the interlayer interactions become stronger when the A-site elements go from Cd to In to Sn and further to Sb. Additionally, it is known that if the crystals of Zr_3CdC_2 and Zr_3SbC_2 are stable, they must meet the requests of thermal, thermodynamic, and mechanical stabilities. Therefore, the thermal stability was quantized by the formation energy:

$$\Delta H = \frac{H_{crystal} - lH_M - mH_A - nH_X}{l + m + n} \quad (1)$$

where M , A , and X are composite elements; l , m , n are the number of each element in the unit cell; $H_{crystal}$ is the enthalpy of the unit cell; and H_M , H_A , and H_X are the corresponding enthalpies of the composite atom in the MAX phases of Zr_3CdC_2 and Zr_3SbC_2 . The calculated formation energies (ΔH) of the Zr_3CdC_2 and Zr_3SbC_2 phases were -1.104 and -1.306 eV/atom, respectively. Therefore, both the formation energies of the Zr_3CdC_2 and Zr_3SbC_2 phases are negative, corresponding to the thermal stability.

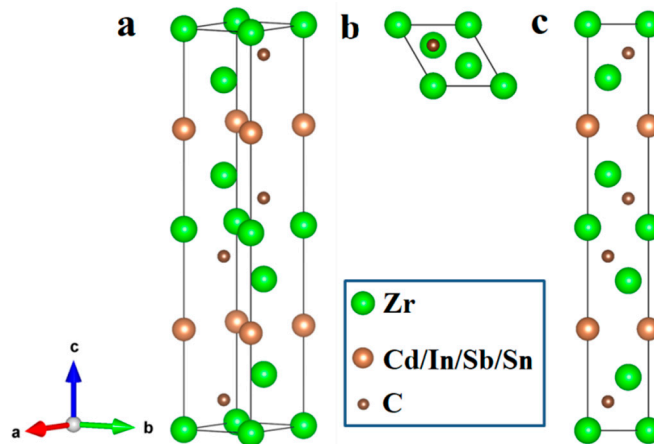


Figure 1. Crystal structures of Zr_3SbC_2 and Zr_3CdC_2 phases: (a) 3-dimensional image, (b) top view image ((0001) plane), and (c) side view image ((1–100) plane).

Table 1. Calculated lattice parameters (\AA) and formation energies (eV/atom) of Zr_3AC_2 ($\text{A} = \text{Cd, In, Sn, and Sb}$) phases.

Phase	a (\AA)	c (\AA)	ΔH (eV/atom)
Zr_3CdC_2	3.319	20.393	-1.104
	3.337	20.251	-1.220
Zr_3InC_2	3.352 [21]	20.252 [21]	
	3.348	19.870	-1.282
Zr_3SnC_2	3.359 [19]	19.876 [19]	
	3.367	19.413	-1.306
Zr_3SbC_2			

Furthermore, the thermodynamic stability of the Zr_3CdC_2 and Zr_3SbC_2 phases was investigated by calculating the phonon dispersion, as shown in Figure 2. The phonon dispersion curve can reflect the dynamic stability of materials to a certain extent. In the first-principles calculation, high symmetry points were selected in the Brillouin zone according to the crystal structure to calculate the mechanical constants. The calculation results showed that there was no negative frequency (imaginary frequency) in the Brillouin zone, which means that the dynamic stability of materials is studied under standard pressure. The minor softness around the Γ and I points are deemed to be caused by the numerical error in calculations but not by the solid-state physics theory. It is observed that Zr_3SbC_2 has a smaller maximum frequency than Zr_3CdC_2 , which means that Zr_3CdC_2 has a higher melting point, i.e., the highest frequency mode is more difficult to activate for Zr_3CdC_2 [29]. The calculated melting point of Zr_3CdC_2 (1548.344 K) is higher than that of Zr_3SbC_2 (1451.880 K). In addition, it is known that the Debye temperature is connected to the lattice vibration, thermal expansion coefficient, specific heat, and melting point of the crystal. As the maximum frequency mode of vibration, the calculated T_D using elastic modulus is specified as one of the standard approaches [30,31]. The calculated Debye temperatures of Zr_3CdC_2 and Zr_3SbC_2 are 392.7 K and 386.2 K, respectively, lower than those of Zr_3InC_2 (488.9 K) and Zr_3SnC_2 (493.7 K).

Table 2. Calculated elastic constants of C_{ij} of Zr_3AC_2 ($\text{A} = \text{Cd, In, Sn, and Sb}$) phases.

Phase	C_{11} (GPa)	C_{12} (GPa)	C_{33} (GPa)	C_{13} (GPa)	C_{44} (GPa)
Zr_3CdC_2	283.717	94.155	228.795	67.108	33.936
Zr_3InC_2	310.372	81.969	248.679	68.846	84.965
Zr_3SnC_2	286.005	109.654	290.242	89.750	118.166
Zr_3SbC_2	239.549	108.369	252.822	126.183	62.190

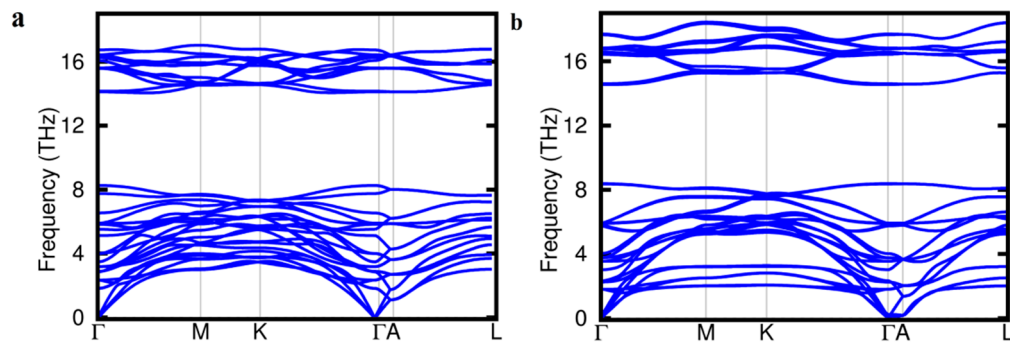


Figure 2. Calculated phonon dispersion of (a) Zr_3SbC_2 and (b) Zr_3CdC_2 phases.

On the other hand, the crystals of Zr_3CdC_2 and Zr_3SbC_2 are also mechanically stable and are confirmed to meet the Born–Huang criteria (Equation (2)), where C_{ij} is presenting the elastic constants and is listed in Table 2 [32]:

$$C_{11} > |C_{12}|, 2C_{13} < C_{33}(C_{11} + C_{12}), C_{44} > 0 \quad (2)$$

It is seen that the pure shear elastic constants of C_{44} are lower than the unidirectional elastic constants of C_{11} and C_{33} . This result means that the shear deformation is easier to occur in comparison with linear compression along the crystallographic *a*- and *c*-axes. The unequal values of C_{11} , C_{33} , and C_{44} ($C_{11} \neq C_{33} \neq C_{44}$) imply different atomic arrangements and hence, different bonding strengths along the *a*-axis, *c*-axis, and shear planes. The combination of C_{12} and C_{13} leads to functional stress along the crystallographic *a*-axis when a uniaxial strain exists in both the *b*- and *c*-axes. The low values of these constants imply that the Zr_3CdC_2 and Zr_3SbC_2 phases will accept shear deformation along the *b*- and *c*-axes when adequate stress is applied to the *a*-axis of the crystals.

3.2. Theoretical Mechanical Properties of Zr_3CdC_2 and Zr_3SbC_2 Phases

In order to clearly understand the mechanical properties of the Zr_3CdC_2 and Zr_3SbC_2 phases, the bulk modulus (B), shear modulus (G), Young's modulus (E), Pugh's ratio, and Vickers hardness (H) were calculated based on the equations (S is the elastic softness constant) [33–41]:

$$B_V = (2(C_{11} + 2C_{12} + 4C_{13} + C_{33})/9) \quad (3)$$

$$B_R = 1/(2S_{11} + 2S_{12} + 4S_{13} + S_{33}) \quad (4)$$

$$G_V = (3.5C_{11} - 2.5C_{12} - 2C_{13} + C_{33} + 6C_{44})/15 \quad (5)$$

$$G_R = 15/(8S_{11} - 10S_{12} - 8S_{13} + 4S_{33} + 6S_{44}) \quad (6)$$

$$B = (B_V + B_R)/2 \quad (7)$$

$$G = (G_V + G_R)/2 \quad (8)$$

$$H_V^G = 0.1769G - 2.899 \quad (9)$$

The calculated bulk moduli, shear moduli, and Vickers hardnesses of the Zr_3CdC_2 and Zr_3SbC_2 phases are listed in Table 3, compared to those of the Zr_3InC_2 and Zr_3SnC_2 phases. Also, the changing tendencies of the bulk moduli, shear moduli, Young's moduli, and Vickers hardness of the Zr_3AC_2 ($A = \text{Cd}$, In , Sn , and Sb) phases are shown in Figure 3. It is seen that the bulk modulus shows a monotonic increase from 137.942 to 160.068 GPa when the A-site element goes from Cd to In and finally to Sn (Figure 3a). For the Zr_3SnC_2 and Zr_3SbC_2 phases, they have larger bulk moduli of 160.068 and 159.913 GPa, respectively. Whereas for the shear modulus, the Zr_3SbC_2 and Zr_3CdC_2 phases have lower values of 61.810 and 62.477 GPa than those of Zr_3InC_2 and Zr_3SnC_2 of 95.251 and 102.306 GPa, respectively. According to the calculated Pugh's ratio, Zr_3CdC_2 (2.208) and Zr_3SbC_2 (2.587) are the ductile phases ($B/G > 1.75$), while Zr_3InC_2 (1.455) and Zr_3SnC_2 (1.565) belong to the brittle phases. As a result,

the Zr_3InC_2 (15.842 GPa) and Zr_3SnC_2 (14.625 GPa) phases have higher Vickers hardnesses than those of Zr_3CdC_2 (5.488 GPa) and Zr_3SbC_2 (4.309 GPa), as shown in Figure 3b.

Table 3. Calculated mechanical moduli of B , E , G , Pugh's ratio of B/G , Vickers hardness of H_V , melting point of T_m , and Debye temperatures of T_D of Zr_3AC_2 ($A = Cd, In, Sn$, and Sb) phases.

Phase	B (GPa)	G (GPa)	E (GPa)	B/G	H_V (GPa)	T_m (K)	T_D (K)
Zr_3CdC_2	137.942	62.477	162.846	2.208	5.448	1548.344	392.7
Zr_3InC_2	144.437	95.251	242.262	1.455	15.842	1658.135	488.9
Zr_3SnC_2	160.068	102.306	253.013	1.565	14.625	1647.378	493.7
Zr_3SbC_2	159.913	61.810	164.265	2.587	4.309	1451.880	386.2

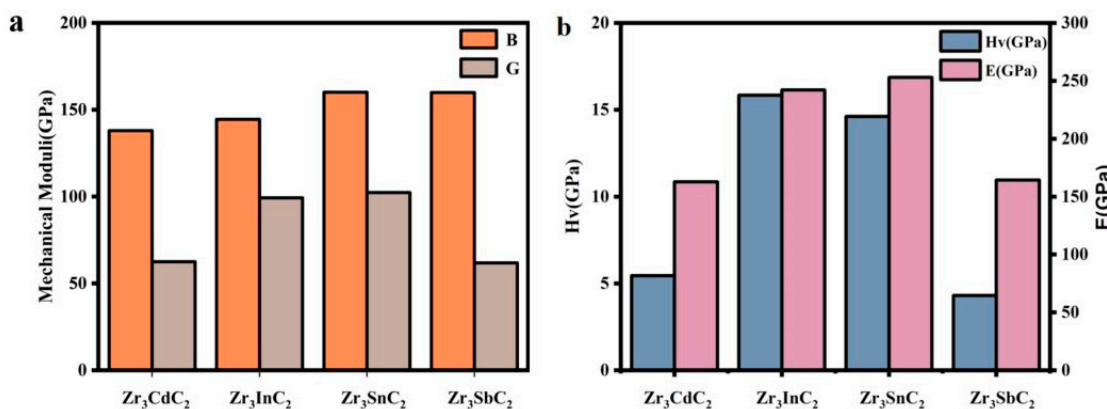


Figure 3. Variation trend of (a) bulk moduli (B) and shear moduli (G), and (b) Young's moduli (E) and Vickers hardnesses (H_V) of Zr_3AC_2 ($A = Cd, In, Sn$, and Sb) phases.

Additionally, the bond length, bond population, and Bader charge (ΔQ) of the Zr_3CdC_2 and Zr_3SbC_2 phases were calculated, as listed in Table 4. Here, Zr1 is an atom far away from the atomic layer A, and Zr2 is an atom near the atomic layer A. It can be seen that the comprehensive bond populations of A-site atoms In (0.87 and 1.24) and Sn (0.87 and 1.23) are all larger than those containing Cd atoms (0.85 and 1.24), indicating that the covalent interaction between Zr and In/Sn elements is strong. Because Zr_3InC_2 and Zr_3SnC_2 crystals have stronger covalent bonds inside, they show a higher elastic modulus and Vickers hardness. Whereas, for the Zr_3SbC_2 phase, though its interatomic population number is larger (0.88 and 1.24), its interatomic bond length (2.384 Å and 2.268 Å) is larger than those of Zr_3InC_2 (2.383 Å and 2.245 Å) and Zr_3SnC_2 (2.380 Å and 2.260 Å). Generally speaking, the longer the bond length, the lower the bond energy and the lower the Vickers hardness. Additionally, the total electron gain/loss of electrons in the crystals of Zr_3CdC_2 (1.692 and 2.726) and Zr_3SbC_2 (1.700 and 2.658) is greater than those of Zr_3InC_2 (1.698 and 2.703) and Zr_3SnC_2 (1.577 and 2.526), which indicates that their ionic properties are stronger and their covalent properties are weaker; that is, their Vickers hardness values are lower than those of Zr_3InC_2 and Zr_3SnC_2 . The relatively high atomic charge transfer indicates the main ionic bond characteristics. The number of charges transferred by Zr1 is higher than that transferred by Zr2, which indicates that its covalence is weak. Interestingly, this conclusion is self-consistent with the long bond length and weak bond energy of Zr1-C [42].

Table 4. The calculated bond length, bond population, and Bader charge (ΔQ) of Zr_3AC_2 ($A = Cd, In, Sn$, and Sb) phases.

Phase	Zr1-C Length (Å)	Zr1-C Population	Zr2-C Length (Å)	Zr2-C Population	ΔQ_{Zr1}	ΔQ_{Zr2}	ΔQ_C
Zr_3CdC_2	2.377	0.85	2.242	1.24	1.591	1.135	-1.692
Zr_3InC_2	2.383	0.87	2.245	1.24	1.592	1.111	-1.698
Zr_3SnC_2	2.380	0.87	2.260	1.23	1.578	0.948	-1.577
Zr_3SbC_2	2.384	0.88	2.268	1.24	1.642	1.016	-1.700

3.3. Synthesis and Microstructure Characterization of Zr_3CdC_2 and Zr_3SbC_2 Phases

Initially, in an attempt to synthesize the Zr_3CdC_2 and Zr_3SbC_2 phases by spark plasma sintering, mixed powders with the molar ratio of Zr:Cd/Sb:C = 3:1.5:1.5 were sintered based on the consideration of easy evaporation of Cd/Sb and C deficiency in the $P6_3/mmc$ hexagonal crystals. Considering the synthesis temperature of Ti_2CdC ($750\text{ }^\circ\text{C}$ [22]), Zr_3InC_2 ($1400\text{ }^\circ\text{C}$ [21]) and Zr_3SnC_2 ($1200\text{ }^\circ\text{C}$ [19]), the sintering temperatures of complexes were initially designed as $850\text{ }^\circ\text{C}$ and $1300\text{ }^\circ\text{C}$, respectively. The examined X-ray diffraction (XRD) patterns acquired from the synthesized samples are displayed in Figures 4a and 5a. In Figure 4a, in combination with the PDF cards, it is determined that a large amount of Zr, ZrC , $ZrCd_2$, and unknown phases exist in the cadmium-containing sample; while, in Figure 5a, it is judged that ZrC , Zr_2Sb_3 , Zr_2Sb , and unknown phases are in the antimony-containing sample. Significantly, in comparison with the theoretical XRD patterns, as shown in Figures 4b and 5b, the (002) and (004) diffraction peak positions of Zr_3CdC_2 and Zr_3SbC_2 have a similar degree of rightward shift. This might be due to the occurrence of crystal defects in the Zr_3CdC_2 and Zr_3SbC_2 phases, resulting in smaller lattice parameters. Anyhow, the (002) and (004) diffraction planes of Zr_3CdC_2 and Zr_3SbC_2 can still be presumed to be in greater accord with the theoretical results. Therefore, it is expected that the Zr_3CdC_2 and Zr_3SbC_2 phases have been synthesized. Furthermore, in order to enhance the purity of the samples, the mixture powders were sintered at different temperatures, and the different molar ratios of the mixture powders were designed and annealed at the optimal temperature for comparison. Figure S1 shows the XRD patterns of the cadmium-containing samples synthesized at $650\text{--}1050\text{ }^\circ\text{C}$ with the molar ratio of Zr:Cd:C = 3:1.5:1.5. And Figure S2 shows the XRD patterns of the antimony-containing samples synthesized at $900\text{--}1400\text{ }^\circ\text{C}$ with the molar ratio of Zr:Sb:C = 3:1.5:1.5. By comparing the XRD patterns in Figure S1, it can be found that only at $850\text{ }^\circ\text{C}$ does the cadmium-containing sample have the least impurity phases, and the XRD pattern is closest to the theoretical result in Figure 4b. Therefore, $850\text{ }^\circ\text{C}$ is considered to be the optimum sintering temperature for the Zr_3CdC_2 phase. Similarly, the optimum sintering temperature for synthesizing the Zr_3SbC_2 phase was determined as $1300\text{ }^\circ\text{C}$. Continuously, for the Zr_3CdC_2 phase, the mixed powders with the molar ratios of Zr:Cd:C = 3:(1.4–1.8):2 were sintered at $850\text{ }^\circ\text{C}$, and the examined XRD patterns are shown in Figure S3. It is seen that no obvious existence of the Zr_3CdC_2 phase could be determined. Then, the molar ratios of the mixture powders were modified to be 3:1.5:(1.5–2.25), and the samples were sintered at the optimum temperature of $850\text{ }^\circ\text{C}$. It is seen that there is no remarkable enhancement of purity of the Zr_3CdC_2 phase, as shown in Figure S4. It seems that the optimal molar ratio is 3:1.5:1.5 to synthesize the Zr_3CdC_2 phase. Similarly, for the Zr_3SbC_2 phase, the mixed powders with the molar ratios of Zr:Sb:C = 3:(1.5–1.95):2 were sintered at $1300\text{ }^\circ\text{C}$. By comparing the XRD patterns of samples sintered with the different molar ratios, the purity of the Zr_3SbC_2 phase was not obviously enhanced, as shown in Figure S5. Therefore, the optimized molar ratio of synthesizing the Zr_3SbC_2 phase is confirmed as Zr:Sb:C = 3:1.5:1.5. Owing to the existence of too many impurities in the sintered samples, it is difficult to refine the obtained XRD patterns by using the Rietveld method. Anyhow, in order to richen the information of the new phases of Zr_3CdC_2 and Zr_3SbC_2 , the theoretical crystal constants, atomic positions, and the XRD data are given and listed in Tables S1–S3.

In addition, in order to characterize the Zr_3CdC_2 and Zr_3SbC_2 grains in the sintered samples, the fracture surfaces of sintered bulks that underwent the shear loading were observed by using the scanning electron microscope, as shown in Figures 6 and 7. Clearly, the grains with a typical nanolaminar character of MAX phases in the sintered bulks are the Zr_3CdC_2 and Zr_3SbC_2 phases (Figures 6a–f and 7a–f), which are the same as other typical MAX phases of Ti_3AlC_2 and Ti_3SiC_2 [43,44]. Obvious bending and twisting phenomena were observed in these grains. Many equiaxed carbide grains are nearby. Additionally, the testing positions of the energy dispersive spectroscopy (EDS) analysis are labeled by white crosses in Figures 6 and 7b,d,f, and the results are displayed in Tables 5 and 6. It is confirmed that the average element ratios are Zr:Cd = 3:0.976 for Zr_3CdC_2 grains and Zr:Sb = 3:1.012

for Zr_3SbC_2 grains, respectively, very close to the ratio of 3:1. Here, no data of the C element was collected, as the EDS analysis could not guarantee the accuracy of the C element.

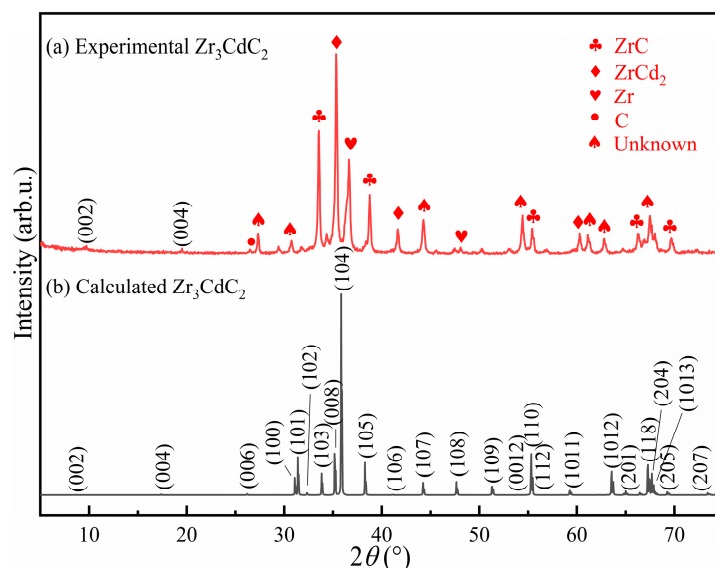


Figure 4. (a) Experimental and (b) theoretically calculated X-ray diffraction (XRD) patterns of Zr_3CdC_2 samples. The sample was synthesized at $850\text{ }^\circ\text{C}$ with the molar ratio of $\text{Zr:Cd:C} = 3:1.5:1.5$.

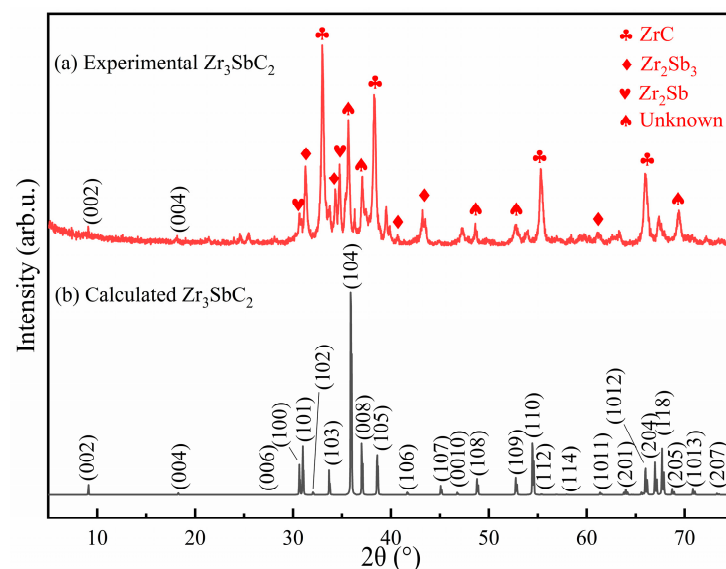


Figure 5. (a) Experimental and (b) theoretically calculated XRD patterns of Zr_3SbC_2 samples. The sample was synthesized at $1300\text{ }^\circ\text{C}$ with the molar ratio of $\text{Zr:Sb:C} = 3:1.5:1.5$.

Table 5. EDS analysis results of Zr_3CdC_2 grains at the test positions in Figure 6b,d,f.

Element	At.% in Figure 6b	At.% in Figure 6d	At.% in Figure 6f
Zr	75.67	75.31	75.38
Cd	24.33	24.69	24.62

Table 6. EDS analysis results of Zr_3SbC_2 grains at the test positions in Figure 7b,d,f.

Element	At.% in Figure 7b	At.% in Figure 7d	At.% in Figure 7f
Zr	74.48	74.10	75.74
Sb	25.52	25.90	24.26

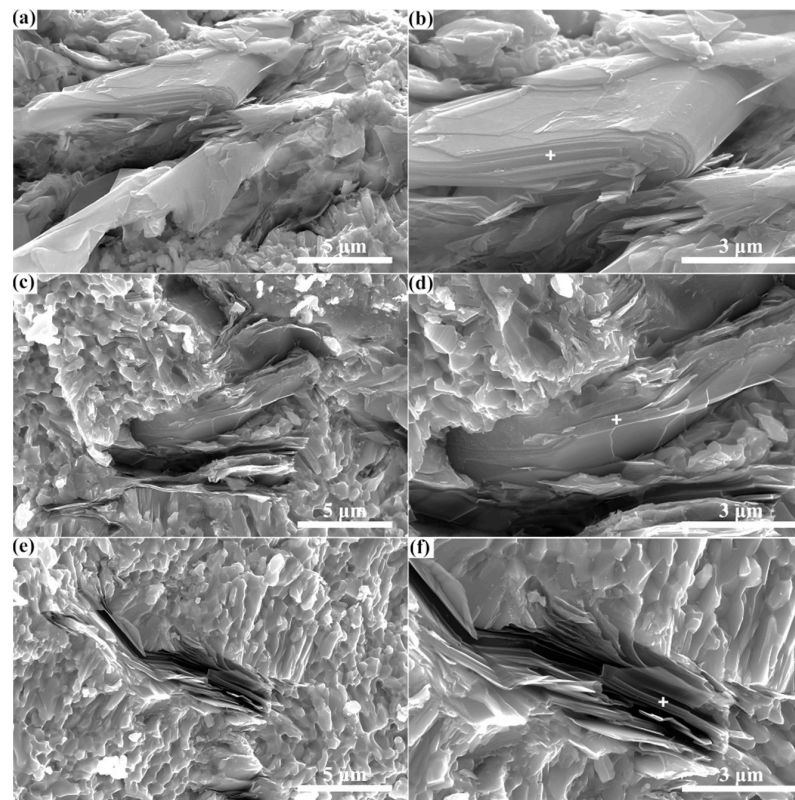


Figure 6. (a–f) Scanning electron microscopy (SEM) images of fracture surface of the Zr_3CdC_2 sample. The testing positions of energy dispersive spectroscopy (EDS) analysis are labeled by white cross in images (b,d,f).

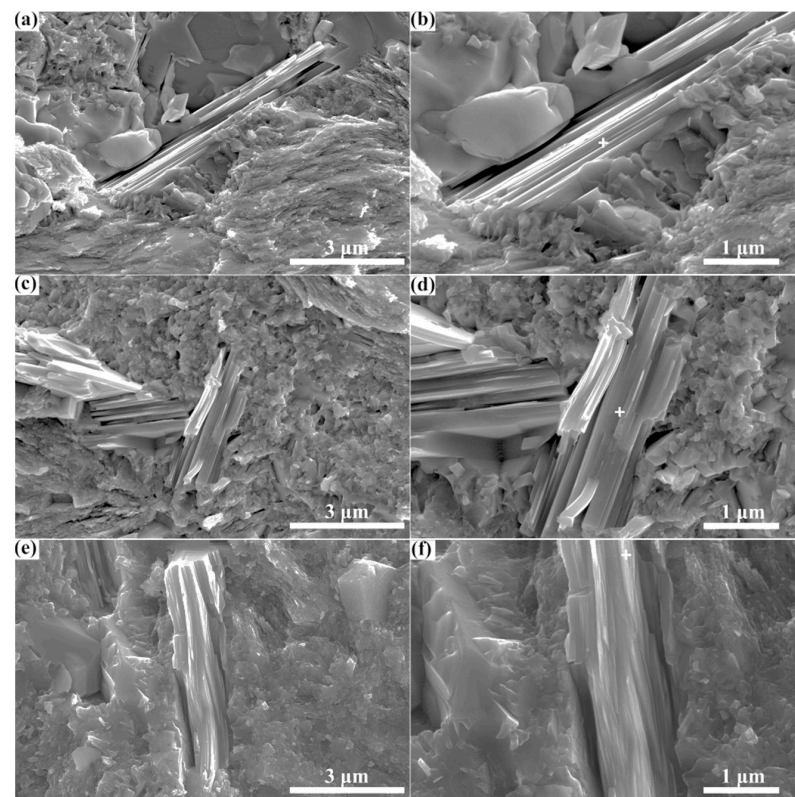


Figure 7. (a–f) SEM images of fracture surface of Zr_3SbC_2 sample. The testing positions of EDS analysis are labeled by the white cross in images (b,d,f).

Therefore, based on the above results, it is believed that the Zr_3CdC_2 and Zr_3SbC_2 phases could stably exist and be successfully synthesized. Combined with the above theoretical calculations, the pure Zr_3CdC_2 and Zr_3SbC_2 MAX phases are shown to have excellent machinability. However, due to the limitation of sintering, it is rather difficult to purify the Zr_3CdC_2 and Zr_3SbC_2 phases, and it is greatly worth it for us to explore new synthesis methods to improve the purity of the two MAX phases.

4. Conclusions

Two new ternary laminar MAX phases of Zr_3CdC_2 and Zr_3SbC_2 were predicted and synthesized. The obtained results are listed as follows:

1. It was confirmed that the Zr_3CdC_2 and Zr_3SbC_2 phases belonged to the space group of $P6_3/mmc$ with the hexagonal crystal structure. The calculated crystal parameters of Zr_3CdC_2 were $a = 3.319 \text{ \AA}$ and $c = 20.393 \text{ \AA}$, and those of Zr_3SbC_2 were $a = 3.367 \text{ \AA}$ and $c = 19.413 \text{ \AA}$. The calculated formation energies of Zr_3CdC_2 and Zr_3SbC_2 were -1.104 and -1.306 eV/atom , respectively, which confirm the thermal stability of the two phases. The absence of imaginary frequencies in the acoustic branches of the phonon band structure and the calculation results using the Born–Huang criterion confirmed the thermodynamic and mechanical stability of the two MAX phases. Additionally, the calculated Young's moduli of Zr_3CdC_2 and Zr_3SbC_2 were 162.846 GPa and 164.265 GPa , respectively. The theoretical Vickers hardnesses of the Zr_3CdC_2 (5.448 GPa) and Zr_3SbC_2 (4.309 GPa) phases were low due to the weaker covalent bonds, exhibiting excellent potential machinability.
2. Through spark plasma sintering, composites containing the Zr_3CdC_2 and Zr_3SbC_2 phases could be synthesized at temperatures of 850°C and 1300°C , respectively. The optimal molar ratio of Zr:Cd/Sb:C was determined as $3:1.5:1.5$. Based on the SEM micrographs, the nanolayered characters of the Zr_3CdC_2 and Zr_3SbC_2 grains were determined. The average element ratios were $\text{Zr:Cd} = 3:0.976$ for Zr_3CdC_2 grains and $\text{Zr:Sb} = 3:1.012$ for Zr_3SbC_2 grains, respectively, very close to the ratio of $3:1$.

Supplementary Materials: The following supporting information can be downloaded at: <https://www.mdpi.com/article/10.3390/ma17071556/s1>. Figure S1: XRD patterns of Zr_3CdC_2 samples with the molar ratio of $\text{Zr:Cd:C} = 3:1.5:1.5$ synthesized at the different sintering temperature: (a) 1050°C , (b) 950°C , (c) 850°C , (d) 750°C , and (e) 650°C . Figure S2: XRD patterns of Zr_3SbC_2 samples with the molar ratio of $\text{Zr:Sb:C} = 3:1.5:1.5$ synthesized at the different sintering temperature: (a) 1400°C , (b) 1300°C , (c) 1200°C , (d) 1100°C , (e) 1000°C , and (f) 900°C . Figure S3: XRD patterns of Zr_3CdC_2 samples synthesized at 850°C with the different molar ratio of Zr, Cd , and C : (a) $3:1.8:2$, (b) $3:1.7:2$, (c) $3:1.6:2$, (d) $3:1.5:2$, and (e) $3:1.4:2$. Figure S4: XRD patterns of Zr_3CdC_2 samples synthesized at 850°C with the different molar ratio of Zr, Cd , and C : (a) $3:1.5:2.25$, (b) $3:1.5:2$, (c) $3:1.5:1.75$, and (d) $3:1.5:1.5$. Figure S5: XRD patterns of Zr_3SbC_2 samples synthesized at 1300°C with the different molar ratio of Zr, Sb , and C : (a) $3:1.95:1.5$, (b) $3:1.8:1.5$, (c) $3:1.6:1.5$, and (d) $3:1.5:1.5$. Table S1: Theoretical crystal parameters and atomic positons of Zr_3CdC_2 and Zr_3SbC_2 phases. Table S2: Calculated data of reflections, 2θ , d -spacing, and intensities of Zr_3CdC_2 phase. Table S3: Calculated data of reflections, 2θ , d -spacing, and intensities of Zr_3SbC_2 phase.

Author Contributions: J.L., B.W. and Q.Z. provided the experimental ideas; J.L. and B.W. conceived and implemented the experiment; F.Z. made the theoretical calculations; L.C., Y.Z., Q.F. and C.H. provided desirable guidance; C.H. provided financial support; J.L. and F.Z. co-wrote the manuscript. All authors have read and agreed to the published version of the manuscript.

Funding: This work was supported by the National Natural Science Foundation of China (52072311) and the Sichuan Science and Technology Program (2022YFH0089). The computations were performed on the High-Performance Computing Platform of Southwest Jiaotong University.

Institutional Review Board Statement: Not applicable.

Informed Consent Statement: Not applicable.

Data Availability Statement: All data that support the findings of this study are available from the corresponding author.

Conflicts of Interest: The authors declare no conflict of interest.

References

1. Barsoum, M.W.; El-Raghy, T. Synthesis and Characterization of a Remarkable Ceramic: Ti_3SiC_2 . *J. Am. Ceram. Soc.* **1996**, *79*, 1953–1956. [[CrossRef](#)]
2. Nowotny, V. Strukturchemie einiger Verbindungen der Übergangsmetalle mit den elementen C, Si, Ge, Sn. *Prog. Solid State Chem.* **1971**, *5*, 27–70. [[CrossRef](#)]
3. Barsoum, M.W.; Radovic, M. Elastic and Mechanical Properties of the MAX Phases. *Annu. Rev. Mater. Res.* **2011**, *41*, 195–227. [[CrossRef](#)]
4. Zhang, Q.; Wen, B.; Luo, J.; Zhou, Y.; San, X.; Bao, Y.; Chu, L.; Feng, Q.; Grasso, S.; Hu, C. Synthesis of new lead-containing MAX phases of Zr_3PbC_2 and Hf_3PbC_2 . *J. Am. Ceram. Soc.* **2023**, *106*, 6390–6397. [[CrossRef](#)]
5. Barsoum, M.W.; El-Raghy, T.; Ali, M. Processing and characterization of Ti_2AlC , Ti_2AlN , and $Ti_2AlC_{0.5}N_{0.5}$. *Metall. Mater. Trans. A* **2000**, *31*, 1857–1865. [[CrossRef](#)]
6. Fattahi, M.; Zarezadeh Mehrizi, M. Formation mechanism for synthesis of Ti_3SnC_2 MAX phase. *Mater. Today Commun.* **2020**, *25*, 101623. [[CrossRef](#)]
7. Hosseini-Zadeh, M.; Mirzaee, O.; Mohammadian-Semnani, H. An investigation into the microstructure and mechanical properties of V_4AlC_3 MAX phase prepared by spark plasma sintering. *Ceram. Int.* **2019**, *45*, 7446–7457. [[CrossRef](#)]
8. Zhang, Q.; Wen, B.; Luo, J.; Zhou, Y.; San, X.; Bao, Y.; Feng, Q.; Grasso, S.; Hu, C. Synthesis of new rare earth containing ternary laminar Sc_2PbC ceramic. *J. Eur. Ceram. Soc.* **2023**, *43*, 1735–1739. [[CrossRef](#)]
9. Zhang, Q.; Zhou, Y.; San, X.; Li, W.; Bao, Y.; Feng, Q.; Grasso, S.; Hu, C. Zr_2SeB and Hf_2SeB : Two new MAB phase compounds with the Cr_2AlC -type MAX phase (211 phase) crystal structures. *J. Adv. Ceram.* **2022**, *11*, 1764–1776. [[CrossRef](#)]
10. Cuskelly, D.T.; Richards, E.R.; Kisi, E.H.; Keast, V.J. Ti_3GaC_2 and Ti_3InC_2 : First bulk synthesis, DFT stability calculations and structural systematics. *J. Solid State Chem.* **2015**, *230*, 418–425. [[CrossRef](#)]
11. Sokol, M.; Natu, V.; Kota, S.; Barsoum, M.W. On the chemical diversity of the MAX phases. *Trends Chem.* **2019**, *1*, 210–223. [[CrossRef](#)]
12. Zhou, Y.; Xiang, H.; Hu, C. Extension of MAX phases from ternary carbides and nitrides ($X = C$ and N) to ternary borides ($X = B$, C , and N): A general guideline. *Int. J. Appl. Ceram. Technol.* **2023**, *20*, 803–822. [[CrossRef](#)]
13. Lapauw, T.; Tunca, B.; Cabioch, T.; Lu, J.; Persson, P.O.; Lambrinou, K.; Vleugels, J. Synthesis of MAX phases in the Hf-Al-C System. *Inorg. Chem.* **2016**, *55*, 10922–10927. [[CrossRef](#)] [[PubMed](#)]
14. Zha, X.-H.; Ma, X.; Du, S.; Zhang, R.-Q.; Tao, R.; Luo, J.-T.; Fu, C. Role of the A-element in the structural, mechanical, and electronic properties of Ti_3AC_2 MAX phases. *Inorg. Chem.* **2022**, *61*, 2129–2140. [[CrossRef](#)] [[PubMed](#)]
15. Nair, V.G.; Birowska, M.; Bury, D.; Jakubczak, M.; Rosenkranz, A.; Jastrzębska, A.M. 2D MBenes: A novel member in the flatland. *Adv. Mater.* **2022**, *34*, 2108840. [[CrossRef](#)] [[PubMed](#)]
16. Zhou, A.; Liu, Y.; Li, S.; Wang, X.; Ying, G.; Xia, Q.; Zhang, P. From structural ceramics to 2D materials with multi-applications: A review on the development from MAX phases to MXenes. *J. Adv. Ceram.* **2021**, *10*, 1194–1242. [[CrossRef](#)]
17. Fu, L.; Xia, W. MAX phases as nanolaminate materials: Chemical composition, microstructure, synthesis, properties, and applications. *Adv. Eng. Mater.* **2021**, *23*, 2001191. [[CrossRef](#)]
18. Zhang, T.; Shuck, C.E.; Shevchuk, K.; Anayee, M.; Gogotsi, Y. Synthesis of three families of titanium carbonitride MXenes. *J. Am. Chem. Soc.* **2023**, *145*, 22374–22383. [[CrossRef](#)] [[PubMed](#)]
19. Lapauw, T.; Tunca, B.; Cabioch, T.; Vleugels, J.; Lambrinou, K. Reactive spark plasma sintering of Ti_3SnC_2 , Zr_3SnC_2 and Hf_3SnC_2 using Fe, Co or Ni additives. *J. Eur. Ceram. Soc.* **2017**, *37*, 4539–4545. [[CrossRef](#)]
20. Hadi, M.A.; Christopoulos, S.-R.G.; Naqib, S.H.; Chroneos, A.; Fitzpatrick, M.E.; Islam, A.K.M.A. Physical properties and defect processes of M_3SnC_2 ($M = Ti, Zr, Hf$) MAX phases: Effect of M-elements. *J. Alloys Compd.* **2018**, *748*, 804–813. [[CrossRef](#)]
21. Zhang, Q.; Luo, J.; Wen, B.; Zhou, Y.; Chu, L.; Feng, Q.; Hu, C. Determination of new α -312 MAX phases of Zr_3InC_2 and Hf_3InC_2 . *J. Eur. Ceram. Soc.* **2023**, *43*, 7228–7233. [[CrossRef](#)]
22. Jeitschko, W.; Nowotny, H.; Benesovsky, F. Die H-Phasen: Ti_2CdC , Ti_2GaC , Ti_2GaN , Ti_2InN , Zr_2InN und Nb_2GaC . *Monatshefte Chem.* **1964**, *95*, 178–179. [[CrossRef](#)]
23. Bai, Y.; He, X.; Li, M.; Sun, Y.; Zhu, C.; Li, Y. Ab initio study of the bonding and elastic properties of Ti_2CdC . *Solid State Sci.* **2010**, *12*, 144–147. [[CrossRef](#)]
24. Roknuzzaman, M.; Hadi, M.A.; Nasir, M.T.; Naqib, S.H.; Islam, A.K.M.A. Structural, elastic and electronic properties of nitride Ti_2CdN phase in comparison with the carbide Ti_2CdC phase from First-principles Study. *J. Phys. Conf. Ser.* **2021**, *1718*, 012019. [[CrossRef](#)]
25. Kresse, G.; Furthmüller, J. Efficient iterative schemes for ab initio total-energy calculations using a plane-wave basis set. *Phys. Rev. B* **1996**, *54*, 11169–11186. [[CrossRef](#)] [[PubMed](#)]
26. Perdew, J.P.; Burke, K.; Ernzerhof, M. Generalized gradient approximation made simple. *Phys. Rev. Lett.* **1996**, *77*, 3865–3868. [[CrossRef](#)] [[PubMed](#)]

27. Grimme, S.; Antony, J.; Ehrlich, S.; Krieg, H. A consistent and accurate ab initio parametrization of density functional dispersion correction (DFT-D) for the 94 elements H–Pu. *J. Chem. Phys.* **2010**, *132*, 154104. [[CrossRef](#)] [[PubMed](#)]
28. Momma, K.; Izumi, F. VESTA 3 for three-dimensional visualization of crystal, volumetric and morphology data. *J. Appl. Crystallogr.* **2011**, *44*, 1272–1276. [[CrossRef](#)]
29. Anderson, O.L. A simplified method for calculating the Debye temperature from elastic constants. *J. Phys. Chem. Solids* **1963**, *24*, 909–917. [[CrossRef](#)]
30. Islam, J.; Hossain, A.K.M.A. Investigation of physical and superconducting properties of newly synthesized CaPd₂P₂ and SrPd₂P₂. *J. Alloys Compd.* **2021**, *868*, 159199. [[CrossRef](#)]
31. Fine, M.E.; Brown, L.D.; Marcus, H.L. Elastic constants versus melting temperature in metals. *Scr. Met.* **1984**, *18*, 951–956. [[CrossRef](#)]
32. Born, M. On the stability of crystal lattices. I. *Math. Proc. Camb. Philos. Soc.* **1940**, *36*, 160–172. [[CrossRef](#)]
33. Pugh, S.F. XCII. Relations between the elastic moduli and the plastic properties of polycrystalline pure metals. *Lond. Edinb. Dublin Philos. Mag. J. Sci.* **1954**, *45*, 823–843. [[CrossRef](#)]
34. Jiang, X.; Zhao, J.; Jiang, X. Correlation between hardness and elastic moduli of the covalent crystals. *Comput. Mater. Sci.* **2011**, *50*, 2287–2290. [[CrossRef](#)]
35. Teter, D.M. Computational Alchemy: The Rational Design of New Superhard Materials. Ph.D. Thesis, Virginia Tech, Blacksburg, VA, USA, 1998.
36. Jiang, X.; Zhao, J.; Wu, A.; Bai, Y.; Jiang, X. Mechanical and electronic properties of B₁₂-based ternary crystals of orthorhombic phase. *J. Phys. Condens. Matter* **2010**, *22*, 315503. [[CrossRef](#)] [[PubMed](#)]
37. Miao, N.; Sa, B.; Zhou, J.; Sun, Z. Theoretical investigation on the transition-metal borides with Ta₃B₄-type structure: A class of hard and refractory materials. *Comput. Mater. Sci.* **2011**, *50*, 1559–1566. [[CrossRef](#)]
38. Chen, X.-Q.; Niu, H.; Li, D.; Li, Y. Modeling hardness of polycrystalline materials and bulk metallic glasses. *Intermetallics* **2011**, *19*, 1275–1281. [[CrossRef](#)]
39. Jamal, M.; Jalali Asadabadi, S.; Ahmad, I.; Rahnamaye Aliabad, H.A. Elastic constants of cubic crystals. *Comput. Mater. Sci.* **2014**, *95*, 592–599. [[CrossRef](#)]
40. Shein, I.R.; Ivanovskii, A.L. Elastic properties of superconducting MAX phases from first-principles calculations: Elastic properties of superconducting MAX phases. *Phys. Status Solidi B* **2011**, *248*, 228–232. [[CrossRef](#)]
41. Wang, X.H.; Zhou, Y.C. Layered machinable and electrically conductive Ti₂AlC and Ti₃AlC₂ ceramics: A review. *J. Mater. Sci. Technol.* **2010**, *26*, 385–416. [[CrossRef](#)]
42. Henkelman, G.; Arnaldsson, A.; Jónsson, H. A fast and robust algorithm for Bader decomposition of charge density. *Comput. Mater. Sci.* **2006**, *36*, 354–360. [[CrossRef](#)]
43. Shuck, C.E.; Han, M.; Maleski, K.; Hantanasisirisakul, K.; Kim, S.J.; Choi, J.; Reil, W.E.B.; Gogotsi, Y. Effect of Ti₃AlC₂ MAX phase on structure and properties of resultant Ti₃C₂T_x MXene. *ACS Appl. Nano Mater.* **2019**, *2*, 3368–3376. [[CrossRef](#)]
44. Wozniak, J.; Petrus, M.; Cygan, T.; Adamczyk-Cieślak, B.; Moszczyńska, D.; Olszyna, A.R. Synthesis of Ti₃SiC₂ phases and consolidation of MAX/SiC composites—Microstructure and mechanical properties. *Materials* **2023**, *16*, 889. [[CrossRef](#)] [[PubMed](#)]

Disclaimer/Publisher’s Note: The statements, opinions and data contained in all publications are solely those of the individual author(s) and contributor(s) and not of MDPI and/or the editor(s). MDPI and/or the editor(s) disclaim responsibility for any injury to people or property resulting from any ideas, methods, instructions or products referred to in the content.